



A Nitinol structure with functionally gradient pure titanium layers and hydroxyapatite over-coating for orthopedic implant applications

J. Lee¹ · S. Akin¹ · J. R. Walsh² · M. B. G. Jun¹ · H. Lee² · Y. C. Shin¹ 

Received: 25 October 2022 / Accepted: 19 August 2023 / Published online: 20 September 2023
© The Author(s), under exclusive licence to Springer Nature Switzerland AG 2023

Abstract

In this study, functionally gradient multi-layer coatings are developed on the Nitinol surface for orthopedic implant applications to eliminate potentially toxic Ni ion release and to improve biocompatibility. Using the direct energy deposition (DED) technique, both the core Nitinol and titanium gradient layers are additively manufactured with high purity. The completely alloyed microstructure without microstructural defects provides superior bonding strength compared to other metal coating techniques that rely on particle-to-particle bonding (e.g., thermal spray and physical/chemical vapor deposition). An additional biomedical over-coating of hydroxyapatite (HA) was deposited on the outer surface of the gradient layer structure using the cold spray technique to enhance biocompatibility without compromising high crystallinity. The resultant bonding strength of HA coating was determined to be 26 MPa, which exceeded the minimum adhesion strength requirement (15 MPa) by the ISO-13779 standard (implants for surgery-HA). The in vitro test on the nickel (Ni) ion release revealed that the Ni release rate from the entire gradient Nitinol structure is very low ($0.036 \mu\text{g}/\text{cm}^2$), which is an order of magnitude smaller than commercial Nitinol orthodontic wires, thereby suggesting a promising potential of the novel Nitinol structure in orthopedic and other implantable applications.

Keywords Biomedical implants · Additive manufacturing · Nitinol · Functionally gradient coating · Biocompatibility

1 Introduction

With the growth in the aging population, there is a renewed focus on improving the quality of life for patients using biomedical implants and materials. It is estimated that more than 90% of people over the age of 40 suffer from bone or joint damage that results in limited mobility and decreased quality of life necessitating joint repair or replacement [1]. Not limited to the elderly, injuries either due to sports or accidents have also led to a rising demand for orthopedic implants among young people [2].

Orthopedic implant materials require several attributes including (i) appropriate mechanical properties, (ii) high corrosion and wear resistance, and (iii) excellent

biocompatibility. However, it is often difficult to satisfy all desired characteristics simultaneously. Stainless steel is one of the most widely used orthopedic implant materials with good mechanical properties (i.e., high tensile strength and fracture toughness) [3] and relatively good biocompatibility [4]. However, stainless steel does not have sufficient corrosion resistance, which can lead to the initiation of a fatigue fracture [5]. In addition, the corrosion of stainless steel can release various metal ions (iron, chromium, nickel, and molybdenum), which can cause inflammatory responses [6]. Due to these reasons, the application of stainless steel implants is limited in scope and duration. Cobalt-based alloys, either Co–Cr–Mo alloy or Co–Ni–Cr–Mo alloy, have excellent corrosion resistance and biocompatibility [7]. With their elastic modulus and ultimate tensile strength almost ten times higher than those of human cortical bones, cobalt-based alloys are suitable for orthopedic applications [1]. However, the material mismatch between the elastic modulus of cobalt-based alloys (220–230 GPa [8]) and human bones (30 GPa [8]) can cause stress shielding and stress concentration, leading to bone resorption, inhibition of bone formation, local irritation, inflammation, vascular

✉ Y. C. Shin
shin@purdue.edu

¹ School of Mechanical Engineering, Purdue University, West Lafayette, IN, USA

² Weldon School of Biomedical Engineering, Center for Implantable Devices, Birck Nanotechnology Center, Purdue University, West Lafayette, IN, USA

compromise, and infection [9]. Titanium-based alloy possesses excellent corrosion resistance, which is more than an order of magnitude greater compared to stainless steel [7]. Especially, titanium-based alloys are suitable for orthopedic implant applications due to their high strength, low density, high specific strength, good corrosion resistance, complete inertness, and enhanced biocompatibility [10]. Nonetheless, the potential risk of stress shielding and stress concentration is still present since the elastic modulus of titanium-based alloys (110 GPa [8]) is far greater than that of human bones.

With respect to stiffness mismatch, Nitinol is an ideal candidate for orthopedic implant applications due to its low elastic modulus (40–75 GPa [11]) comparable to human bones (30 GPa [8]). In addition, Nitinol has other desirable characteristics suitable for orthopedic implant applications such as super elasticity, shape-memory property, bending and corrosion resistance, fatigue resistance, magnetic resonance compatibility, and kink resistance [12].

For a broader adoption of Nitinol for orthopedic implant applications, additional functional improvements are necessary. First, the corrosion resistance of Nitinol needs to be enhanced. Corrosion of Nitinol leads to Ni ion release from the surface, which can cause an allergic symptom in the human body [13, 14]. While some studies showed promising aspects of Nitinol in their *in vitro* and short-period *in vivo* tests, wherein the Ni ion release rates decreased to a nearly negligible level after a few days of the experiment, long-term effects after implantation need to be considered for orthopedic implant applications. Kamachimudali et al. [2] claimed that fretting corrosion can occur from two opposing surfaces (such as bone plates and screw heads) rubbing each other in an oscillating fashion in the body environment. Moreover, corrosion slowly occurs from the metal surface due to galvanic electrochemical reactions after implantation in a human body. Implant materials are in contact with extracellular body fluids that contain chloride ions, which can corrode metallic materials. Li et al. [15] tested untreated Nitinol for 2 years using an animal model and claimed that the Ni release from the untreated Nitinol at the initial stage of implantation is one of the important factors that caused relatively low biocompatibility and resulted in immature osseous lamella structure and slow osteointegration at the interface.

In addition to corrosion resistance, the hard tissue compatibility of Nitinol also needs to be better characterized for orthopedic implant applications. In fact, the biocompatibility of Nitinol itself is moderate and there are promising results regarding the cytotoxicity of Nitinol that is comparable to titanium and stainless steel. Ryhänen et al. [16] showed that the proliferation of *in vitro* osteoblasts on the surface of Nitinol was comparable to that of ASTM grade 2 pure titanium and stainless steel 316. Ryhänen et al. [17] studied *in vivo* biocompatibility of Nitinol after intramuscular

and perineural implantation in rats for 26 weeks. The results showed that the thickness of the capsule membrane formed on Nitinol was comparable to those of stainless steel and Ti6Al4V. Another *in vivo* biocompatibility study by Ryhänen et al. [18] showed that the formation of fibroblast-like cells around Nitinol after 26 weeks of periosteal implantation was comparable to stainless steel and Ti6Al4V. Wever et al. [19] showed that cytotoxicity, sensitization, and genotoxicity test results of Nitinol were no different from the widely used implant material, AISI 316LVM stainless steel. Trépanier et al. [20] showed good cytocompatibility of surface-treated Nitinol from *in vitro* proliferation tests using fibroblast human cells, and no adverse effect was observed from surface-treated Nitinol after 12 weeks of *in vivo* implantation. Ayers et al. [21] showed evidence of fibrovascular tissue influx and concomitant bone formation from porous Nitinol implants after 6 weeks of implantation in rabbits.

Despite these successes, reports on Nitinol's potential negative impacts as an implant material should not be neglected since long-term follow-up data are yet not available. Wataha et al. [22] conducted *in vitro* biocompatibility test and showed that Nitinol caused IL-1 β release to indirectly induce ICAM-1 on endothelial cells, which can lead to latent inflammation. Shih et al. [23] showed that Ni ion release from corroded Nitinol was toxic to the primary cultured rat aortic smooth muscle cells. Also, the level of cell growth inhibition was correlated with Ni ion concentration from *in vitro* cell cultivation tests.

Applications of Nitinol in implants have been limited due to its high toughness and low machinability, which result in a high manufacturing cost in achieving requisite shapes [24]. As an alternative solution, additive manufacturing (AM) techniques have received much attention since they can easily achieve the personalized design and material properties for each patient and use. The feasibility of producing Nitinol parts has been studied using many AM techniques, including direct metal deposition [25–27], selective laser melting (SLM) [28], selective laser sintering (SLS) [29, 30], electron beam melting (EBM) [31–33], and direct energy deposition (DED) [34, 35]. By controlling the nickel content and post-heat treatment conditions, studies showed that the properties of AM-printed Nitinol (phase transformation temperatures [36, 37] and mechanical properties [37–39]) can be tailored to meet specific orthopedic needs.

In this study, the DED technique, which is suitable for building defect-free microstructure and achieving precise composition from its customizable powder feed rate, was used to build both the core material, Nitinol, and the functionally gradient Ti coating layer without microstructural defects. The core Nitinol was produced with proper DED operating parameters, composition, and post-heat treatment conditions that were already investigated in the authors'

previous study [37]. The elastic modulus of the DED Nitinol in this study was selected as 60 GPa which is close to that of human bones (30 GPa [8]) to avoid severe stiffness mismatching with human bones. The functionally gradient Ti layer was then deposited on the surface of Nitinol with 0% nickel composition at the top layer to significantly suppress nickel release. Lastly, additional biocompatible ceramic material, hydroxyapatite (HA), was over-coated using a cold spraying technique to further enhance the biocompatibility of the as-fabricated titanium–Nitinol surface. The resultant gradient functional coating was systematically studied in terms of microstructure, chemical composition, and adhesion strength. Moreover, the Ni ion release rate was measured in vitro for three different surfaces: (i) Nitinol, (ii) Ti gradient coating on Nitinol, and (iii) HA over-coating on Ti gradient coating to demonstrate the anti-corrosion property of the novel Nitinol structure.

2 Structure design and experimental procedures

2.1 Overall structure design

The entire structure is composed of three parts: (i) Nitinol as core material, (ii) Ti gradient structure on Nitinol, and (iii) biocompatible over-coating of HA on the Ti layer. For demonstration purposes, an example of a femoral implant was designed utilizing the Nitinol gradient structure, as shown in Fig. 1. The core material is a dense (over 99%) Nitinol without microstructural defects. With high purity, all the advantageous features of Nitinol as an orthopedic implant can be exploited [40]. The Nitinol surface is fully covered with a dense thin layer of Ti gradient coating to eliminate

the possibility of Ni ion release (i.e., 0% Ni composition at the outer layer) while achieving the highest bonding strength due to the completely alloyed microstructure. The final (top) outer surface is then coated with a biocompatible material (HA) using a cold spraying technique to enhance corrosion resistance and the tissue compatibility of the overall structure. The following subsections discuss each structural layer shown in Fig. 1.

2.1.1 Nitinol as core

The core Nitinol layer was produced using the DED technique through the OPTOMECH LENS 750 system equipped with a fiber laser (wavelength of 1064 nm, maximum power of 500W and focal diameter of 660 microns). The processing parameters of the DED manufactured Nitinol were described in the previous study of the authors [37], which discussed the mechanical properties of the DED Nitinol according to its composition and post-heat treatment history (Table 1 [37]). The Nitinol in a fully dense form was deposited with the laser power of 250 W, a scanning speed of 12.5 mm/s, and a hatch spacing of 0.5 mm. For each layer, six different hatch orientation angles were applied in a sequence order: n th layer: 0° , $n + 1$ th layer: 60° , $n + 2$ th layer: 120° , $n + 3$ th layer: 180° , $n + 4$ th layer: 240° , and $n + 5$ th layer: 300° . Two separate powder feeders filled with pure (over 99.9%) nickel and titanium powders were controlled independently to achieve the arbitrary composition of Nitinol. Nickel and titanium powders in a size range of 45–150 μm were acquired from Atlantic Equipment Engineers and Advanced Powders & Coatings, respectively. Argon was used as powder carrier gas and shield gas around the melt pool. The oxygen level was maintained at less than 20 ppm during the DED process. The schematic of the DED process is shown in Fig. 2.

Powder feed rates of nickel (3.6 g/min) and titanium (5.6 g/min) powders were controlled for the target composition of 51.3% (at.), and all Nitinol samples were solution heat treated at 1050 $^\circ\text{C}$ for 10 h under an argon environment to achieve the reported elastic modulus of 60 GPa [39]. Compared to other widely used implant materials with high

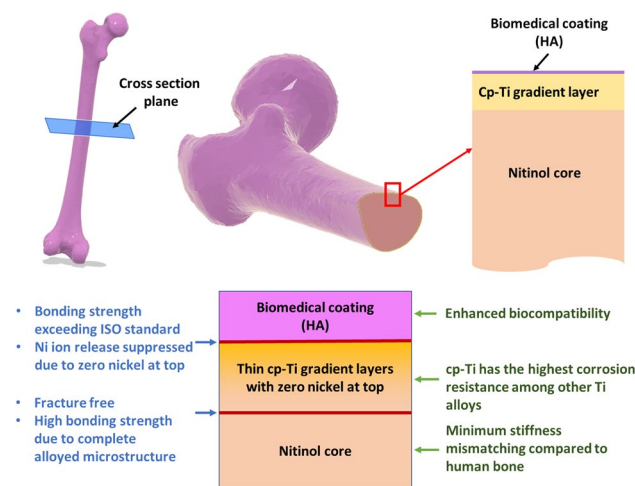
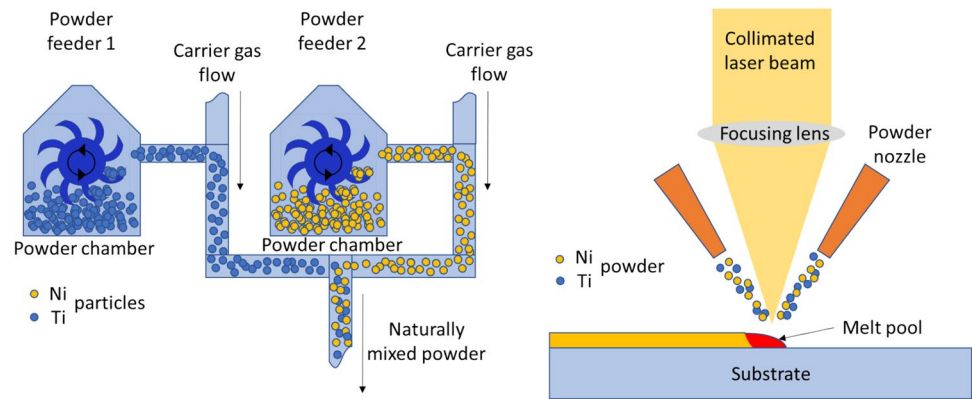


Fig. 1 A potential orthopedic implant application using the Nitinol structure with gradient Ti layers and HA over-coating

Table 1 The DED operating parameters for Nitinol core [37]

Parameters	Value
Laser power	250 W
Scanning speed	12.5 mm/s
Hatch spacing	0.5 mm
Layer thickness	0.25 mm
Hatch orientation	0° , 60° , 120° , 180° , 240° , and 300°
Carrier gas (Ar) flow rate	5 lpm ($8.33 \times 10^{-5} \text{ mm}^3/\text{s}$)
Shield gas (Ar) flow rate	30 lpm ($40.0 \times 10^{-5} \text{ mm}^3/\text{s}$)
Oxygen level in the system	Less than 20 ppm

Fig. 2 Schematic of the DED technique. Un-mixed nickel and titanium powders are loaded into separate powder feeders with independent feed rate control. Naturally mixed powder is delivered to the molten pool



elastic modulus values such as titanium/titanium alloys (110 GPa [8]) or stainless steel (200 GPa [8]), a low elastic modulus of the DED Nitinol is more suited for preventing the stiffness mismatch with the human cortical bone (30 GPa [8]), thereby making the DED technique as a suitable method for producing Nitinol samples with customized mechanical properties.

2.1.2 Gradient Ti layer deposition

A promising method of eliminating the Ni ion release from the surface is to create the final outside layer that is free of Ni elements. In this regard, the outside layer material should be carefully selected so that it does not raise extra cytotoxicity concerns. Titanium and its alloys are generally suitable candidates for clinical applications due to their low corrosion rate. As such, in this study, commercially pure Ti (cp-Ti) was selected as the outside layer material since it has been shown to have the lowest corrosion rate among titanium alloys [8, 41]. Specifically, the cp-Ti showed a lower corrosion resistance compared to Ti6Al4V. Priyadarshini et al. [8] reported a study on the corrosion-resistance behavior of titanium alloys carried out in Hank solution, and they found that the cp-Ti had the lowest corrosion rate followed by Ti6Al4V. Kuphasuk et al. [41] measured corrosion rates among titanium alloys and showed that the cp-Ti had the lowest corrosion rate of 0.012 MPY (mils per year) while Ti6Al4V and NiTi showed 0.0683 MPY and 0.0707 MPY, respectively. In addition, Ti6Al4V contains extra elements (Al and V) that can form unwanted phases if alloyed with Ni and Ti. Therefore, cp-Ti can be considered to be the best choice as the outside coating material.

The gradient layer structure (from NiTi to 100% Ti) has advantages over ordinary coating, especially for its high coating strength. The gradient structure provides the maximum coating strength due to its gradual change in alloyed microstructure. On the other hand, other coating techniques (ex. cold spray [42], plasma spray [43], and electrophoretic deposition [44]) create microstructure with porosity, which

is vulnerable to fatigue crack. Furthermore, its coating strength depends on the molecular adherence force, which is not comparable to that of alloyed microstructure. In this study, the DED technique was used to create gradient layers with dense and defect-free microstructure on the Nitinol surface.

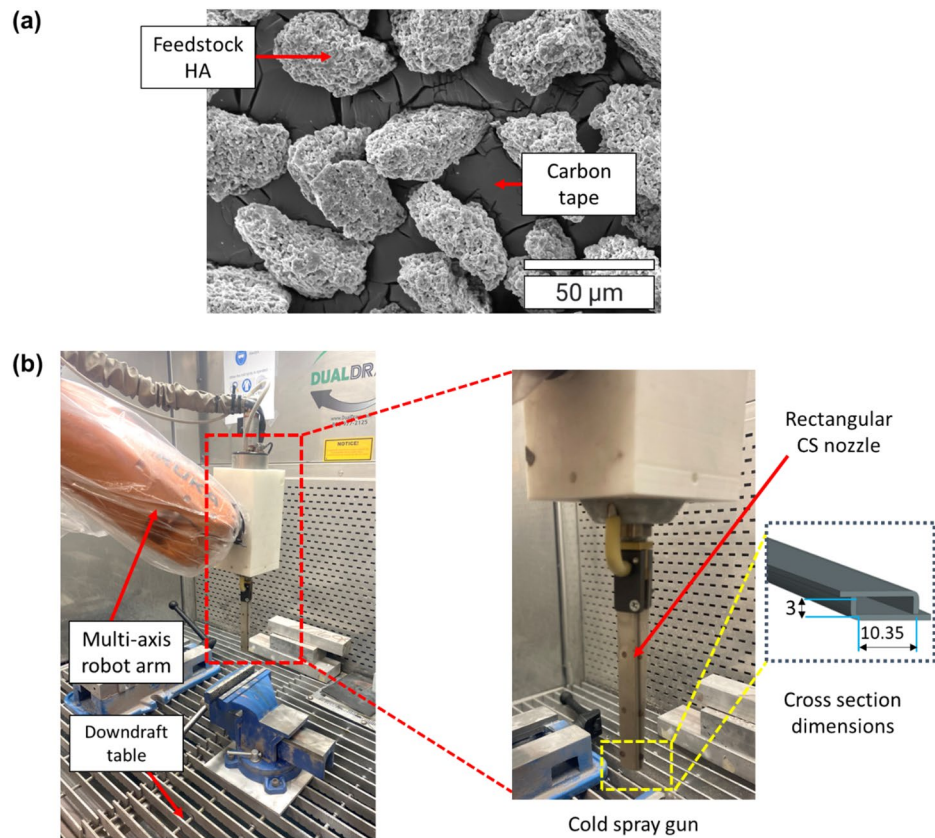
2.1.3 HA over-coating via cold spray

In this study, the cold spray (CS), which is an emerging solid-state material consolidation technique, was employed to deposit the hydroxyapatite (HA) particles on the cp-Ti surface to accomplish HA coating with high crystallinity. It was already demonstrated that the CS technique can achieve HA coating on a titanium surface with high crystallinity [45, 46] and excellent biocompatibility [45].

The crystallinity of HA should carefully be considered since some studies showed that the osteoconductive property of HA with amorphous or low crystallinity was superior to highly crystalline HA [47, 48]. On the other hand, other studies showed superior direct soft tissue attachment from highly crystalline HA compared to HA with lower crystallinity [49, 50]. While there are conflicting reports on the effects of HA crystallinity on osseointegration, it is well-established that HA with high crystallinity provides more desirable long-term osteoconductive properties [50, 51]. Unlike the CS technology, the DED technique is not a proper method for achieving high crystalline HA over-coating since it can easily involve the melting of HA as well as the melting of the substrate material, cp-Ti, which will lead to the formation of undesirable alloyed material.

The final outer surface (i.e., Ni + gradient Ti) was over-coated with hydroxyapatite (HA) by cold spraying to enhance biocompatibility. The irregular-shaped HA powders having a size distribution of 15–45 μm were procured from Medicoat, France. For a clear image acquirement, the feedstock HA particles were placed on a carbon tape during SEM analysis as shown in Fig. 3a. A low-pressure CS machine (Rus Sonic Technology, Inc. K205/407R), as

Fig. 3 **a** SEM image of feedstock HA particles on a carbon tape **b** cold spray experimental setup with a rectangular nozzle and its IR camera image



shown in Fig. 3b, was employed in HA particle deposition experiments. A rectangular-shaped nozzle was used to process a large-area coating owing to its larger exit aperture (i.e., 3 mm × 10.35 mm) compared to the traditional axisymmetric CS nozzles, which generally have a diameter of 4–10 mm [52, 53]. The CS nozzle was mounted on a programmable multi-axis robot arm to precisely control the spraying process in a pre-programmed manner. Compressed air was used as the driving gas in the CS experiments by setting its inlet pressure (gauge) to 0.7 MPa. The driving gas (air) flow was preheated before spraying, and the gas temperature was measured as 150 °C from the outer walls of the nozzle's diverging section using a type K thermocouple (Hanna instruments). The associated infrared (IR) camera (FLIR A300, FLIR System) image of the nozzle is also given in Fig. 3b. After preheating the driving gas flow, the feedstock HA particles as received without any further treatment were radially injected into the divergent section of the nozzle at room temperature. The CS experiments were conducted under the spraying settings presented in Table 2. As for the substrates, two different cp-Ti surface conditions (i.e., face milled and sandblasted) were tested to investigate the effects of surface conditions on the characteristics of cold-sprayed HA coating in terms of microstructure, chemical composition, and adhesion strength.

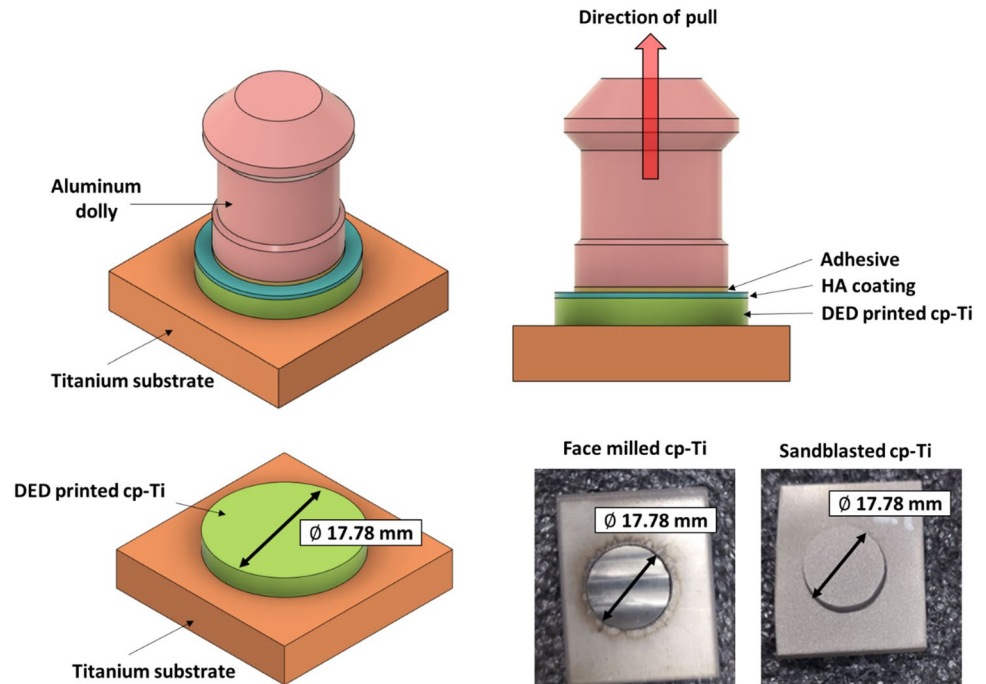
Table 2 Cold spray process parameters used in the experiments

Parameters	Value
Driving gas	Air
Driving gas pressure (MPa)	0.7
Driving gas temperature (°C)	150
Powder feed rate (g/s)	0.2
Nozzle transverse speed (mm/s)	5
Spray distance (stand-off distance) (mm)	20
Number of sprayed layer	1

2.2 Tensile pull-off testing

The adhesion strength of the resulting biomedical coating (HA) was evaluated by the pull-off tensile test according to the ASTM D4541 standard [54], which is a well-established quantitative method to properly characterize the coating strength [55–58]. An adhesion tester (Elcometer 506) shown in Fig. 4 was used to characterize the interfacial adhesion strength between the substrates and the resultant HA coatings. In this regard, the test dollies having a diameter of 14.2 mm were first sanded using a sandpaper to facilitate the intrusion of the glue into the dolly's surface by increasing the dolly's surface roughness. The dollies were then glued on the HA-coated specimens using an epoxy-based adhesive

Fig. 4 Tensile pull-off testing rig and two different surfaces for the pull-off test, face milled and sandblasted



(3M DP460). Before the test, the adhesive was cured at a temperature of 45 °C for 4.5 h. Lastly, the HA coating was pulled off by the applied tension load using the adhesion tester. Note that, for the pull-off adhesion tests, the specimen surfaces were completely over-coated through the cold spraying of HA.

To achieve the maximum coating strength and to investigate the effects of surface condition on characteristics of cold-sprayed HA coating, two different cp-Ti surface conditions (i.e., face milled and sandblasted) were considered. The cp-Ti layers were deposited on a titanium substrate surface by DED, and its surfaces were face milled using a CNC milling machine, as shown in Fig. 4. The sandblasted surface was created using a sandblaster (Cyclone FT-6035) equipped with an abrasive garnet (80 HPA). After sandblasting, all surfaces were cleaned with acetone followed by methanol to remove contaminants. For each surface condition (face milled and sandblasted), five adhesion strength

measurements were recorded to obtain a statistically representative average value with standard deviations.

2.3 Metal ion leaching measurement

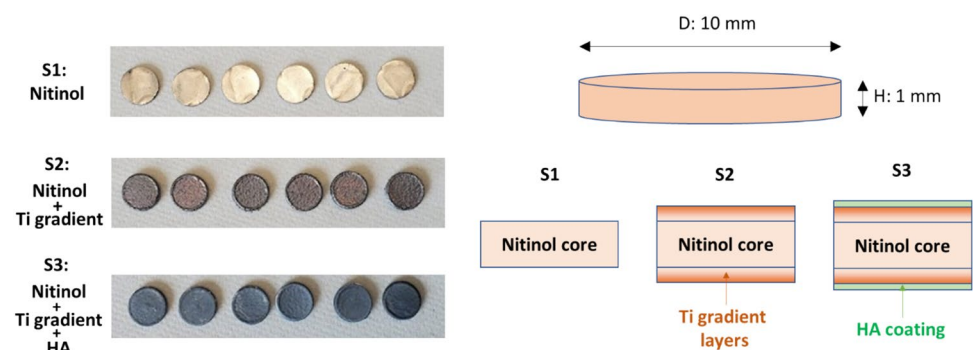
2.3.1 Sample preparation

A total of three different samples were prepared for nickel ion leaching tests, and sample designs are shown in Fig. 5: (i) Nitinol (S1), (ii) Nitinol with Ti gradient layers on top and bottom (S2), and (iii) S2 with HA coatings on top and bottom (S3). Disks with a diameter of 10 mm and a height of 1 mm were selected as S1 samples.

2.3.2 Measurement procedure

The FDA recommends that Nitinol implants be tested for nickel ion release in biological conditions [59]. Thus, a

Fig. 5 Nickel ion leaching test samples



modified version of ASTM F3306 was used to assess the release of nickel from the samples. Invitrogen 10x PBS buffer (Thermo Fisher Scientific, Cat # AM9625) was diluted to 1× concentration using filtered deionized water. Six S1, S2, and S3 samples, as shown in Fig. 5, were placed in 15 ml tubes with 3 ml of 1× PBS. Over 30 days, the samples were moved to fresh PBS every 3 days. The nickel levels from PBS were measured using a Thermo Scientific Elements II ICP-MS. Testing was done on a 10× dilution of the PBS with 400 µl of nitric acid (70%) added to the samples to make the matrix and 50 µl of 1 ppm. In-115 was added as an internal control. The nickel standard used was 10 µg/ml nickel from Inorganic Ventures (MSNI-10PPM-125ML).

2.4 Microstructure analysis

The microstructure was analyzed using a scanning electron microscope (SEM), an optical microscope (OM), and X-ray diffraction (XRD). Before SEM analysis, all samples were sectioned and mounted into bakelite. The bakelite samples were roughly polished using silica abrasive papers in the sequence of 320, 400, 600, and 800 grits. Subsequent fine polishing was done using a 6 µm diamond paste, followed by 0.05 µm colloidal silica. The JEOL 6400 SEM equipped with energy-dispersive X-ray spectroscopy (EDS) was used to analyze surface morphology and chemical composition at target points and regions on sample surfaces. The Bruker D8-FOCUS XRD with a CuKα X-ray source was used with the scanning of 2θ values from 20° to 90° at the rate of 8°/min.

3 Results and discussion

3.1 Nitinol core

All the advantageous features of Nitinol come from the NiTi phase, and therefore a high level of purity is necessary for orthopedic implant applications. The back-scattered SEM image of DED-printed Nitinol is shown in Fig. 6a. The EDS result showed the composition was Ni 51.3% and Ti 48.7% without any other elements. The bright and dark phases in Fig. 6 are NiTi and NiTi₂, respectively. The amount of NiTi₂ was 4% from the DED-printed microstructure while other additive manufacturing techniques such as SHS (selective heat sintering), SPS (spark plasma sintering), HIP (hot isostatic pressing), and SLS-SHS (selective laser sintering–selective heat sintering) created greater amounts of NiTi₂ phase, ranging from 11.8 to 46% [37]. The XRD result of DED-printed Nitinol exhibited only NiTi and NiTi₂ phases, as shown in Fig. 6b.

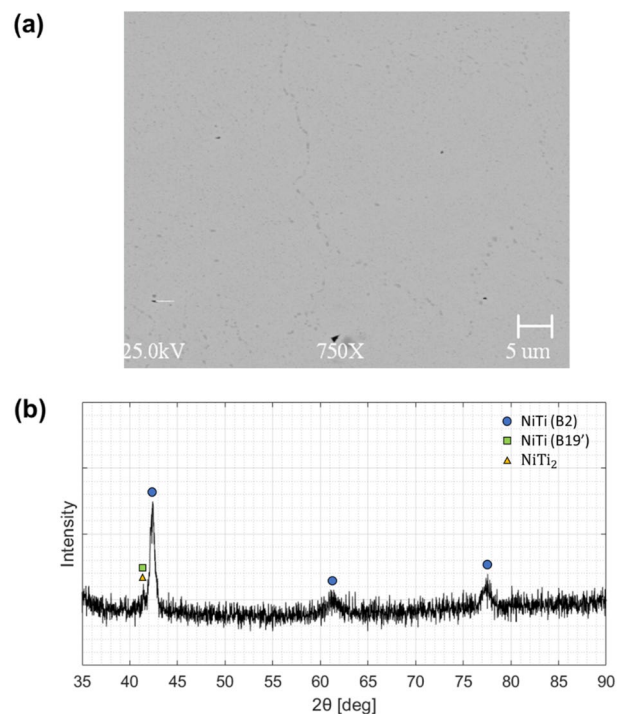


Fig. 6 **a** Back-scattered SEM image of Nitinol, **b** XRD result of DED Nitinol (Ni 51.3%)

3.2 Ti gradient layers

The major purpose of the Ti gradient layer is to achieve (i) defect-free microstructure and (ii) 100% Ti composition at the outer layer. Figure 7a shows the cross-section SEM image of the bio-test sample with Ti gradient layers on the top and bottom of the Nitinol core. It should be noted that no defects (pores and cracks) were observed throughout the Ti gradient layers and NiTi core. At the boundary of the NiTi core and the gradient Ti layers, a thin layer of the NiTi₂ (bright contrast) with a thickness of ~20 µm was formed. As more Ti layers were deposited, a decreasing amount of bright NiTi₂ was observed in the matrix of Ti (dark contrast). The distribution of Ni composition along the vertical direction (from top to bottom) is shown in Fig. 7b. A gradual decrease in Ni composition was observed from the EDS measurement along the building direction from the NiTi core to the outer Ti gradient layer. The 0% Ni composition at the final surface of the Ti gradient layer shows the Ni element was completely absent at the surface. In this study, different laser parameters were tested to achieve the interface layer with the thinnest thickness and defect-free microstructure. While the thickness of the interface layer (composed of highly dense NiTi₂) was increased to 400 µm with higher laser power, the overall thickness of the entire Ti gradient layer was reduced to 500 µm with the thinnest interface layer of

Fig. 7 **a** SEM images of Nitinol core and Ti gradient layer structure, **b** Ni composition distribution along the building direction (from top to bottom)

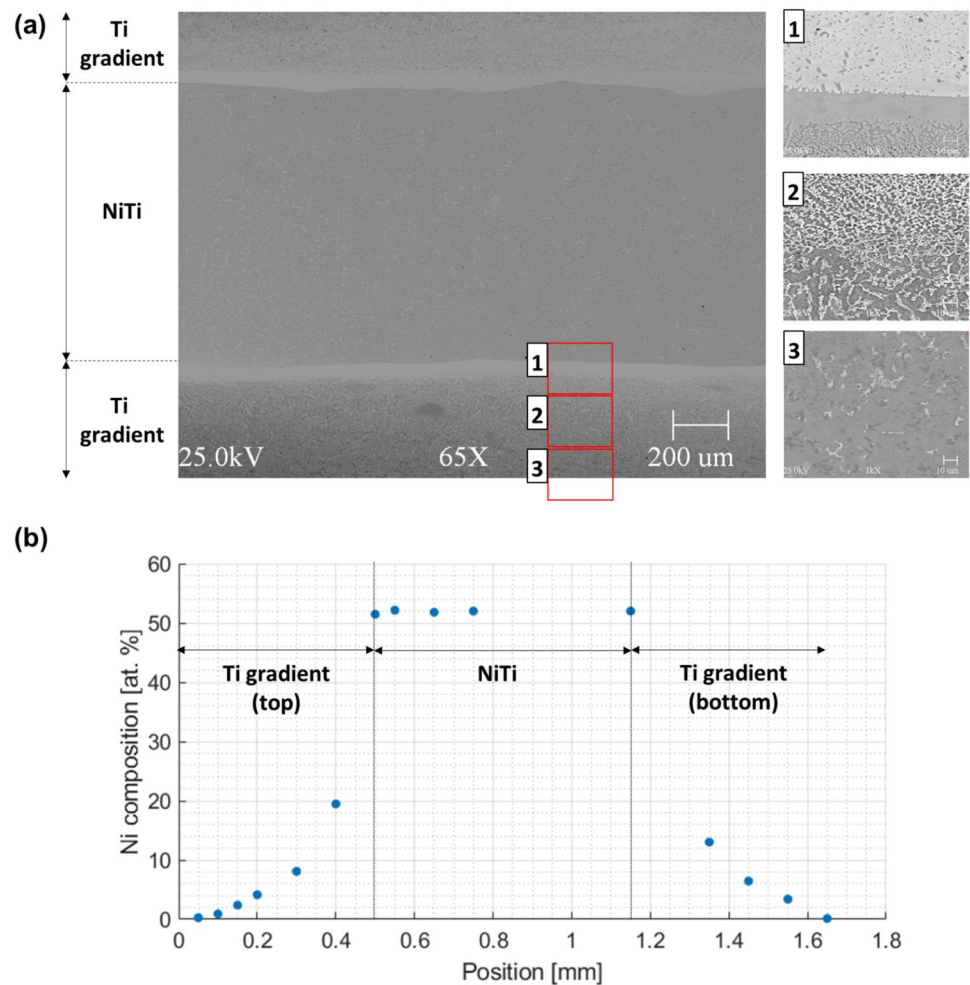


Table 3 The DED operating parameters for the Ti functional gradient layer

Parameters	Value
Laser power	80 W
Scanning speed	12.5 mm/s
Hatch spacing	0.18 mm
Layer thickness	0.1 mm
Hatch orientation	0°, 60°, 120°, 180°, 240°, and 300°

20 μm by choosing the optimized operating parameters. The optimized operating parameters for the Ti functional gradient layer are shown in Table 3. The overall coating thickness of 0.5 mm will have negligible effects on the overall bulk mechanical properties, since it is much less than the dimension of the core NiTi. For example, Zhang et al. [60] created functional–structural NiTi/HA composite with an HA coating thickness in the range of 3.2–3.9 mm. Even with the larger thickness (eight times

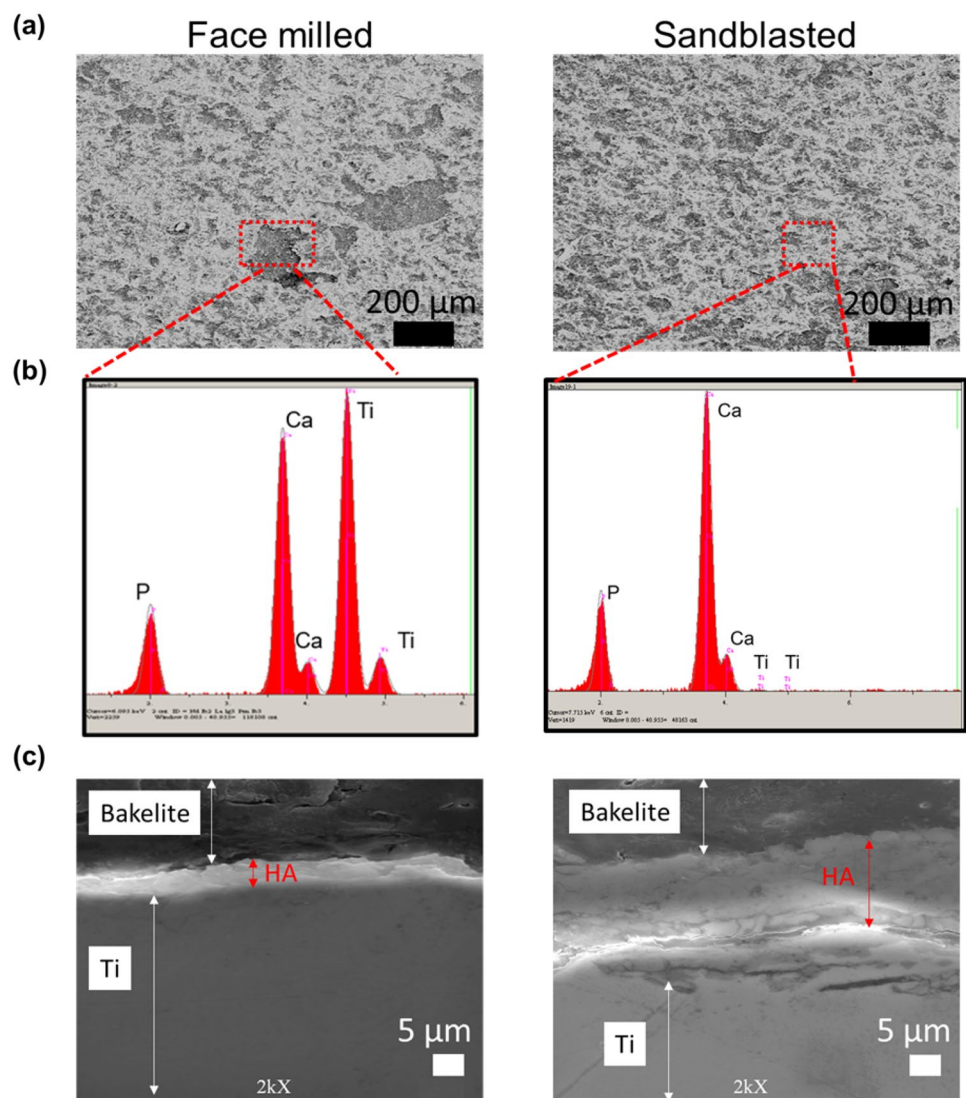
thicker), the superelasticity and mechanical properties of core Nitinol from compression stress–strain responses did not deteriorate.

The microstructure of the NiTi core and the adjacent Ti layers was compared to the previous study by Abioye et al. [61]. The study achieved alloyed microstructure between cp-Ti and Nitinol using the direct laser metal deposition (DLMD) technique. While a similar thickness of the NiTi₂ interface layer was formed, the NiTi layer consisted of a dendrite-shaped NiTi phase in the matrix of NiTi₂, which indicates a low purity of NiTi. In comparison, this study achieved a Nitinol core with a high purity that allowed beneficial mechanical properties for orthopedic implant applications.

3.3 HA over-coating on Ti surface

Cold spray (CS) deposition of HA particles on cp-Ti surfaces was performed using the operational settings listed in Table 2. Figure 8a shows the surface SEM images of the as-cold-sprayed surfaces on the face-milled and sandblasted

Fig. 8 **a** Surface morphology of the HA coating on face-milled (left panel) and sandblasted (right panel) specimens; **b** EDS map of the HA coating on face-milled (left panel) and sandblasted (right panel) specimens; **c** cross-section SEM image of the HA face milled (left panel) and sandblasted (right panel) samples



cp-Ti surfaces. The HA coating with micro-roughness was achieved on both surfaces, which is crucial to trigger cell attachment in orthopedic implant applications. However, severe porosities locally appeared on the face-milled cp-Ti surface, which indicates a non-uniform coating on the face-milled cp-Ti sample. Conversely, a relatively dense HA coating with less porosity was obtained on the sandblasted cp-Ti surface. The reason lies in that direct CS deposition and coating build-up on smooth surfaces is challenging due to the inherent bow-shock region formed near the target surface [62–64]. The substrate surface can be pre-treated for the CS process by increasing the target surface roughness using processes such as sandblasting and grinding, which would further help to alleviate the effect of the bow-shock phenomenon [62].

The EDS analyses, as shown in Fig. 8b, exhibit apparent peaks of phosphorus (P) and calcium (Ca), which were observed on both HA-coated cp-Ti surfaces, indicating a

successful CS deposition of HA particles. A sharp titanium (Ti) peak, however, was observed on the locally porous region of the face-milled surface. It is attributed to the locally formed relatively thin coating that did not fully cover the titanium surface.

The cross-sectional morphology of the resultant HA coatings was also analyzed. As seen in Fig. 8c, the sandblasted cp-Ti surface resulted in a considerably thicker HA coating (i.e., ≈ 3 times thicker than the face-milled surface). This result suggests that post-processing of the 3D printed Ti parts via sandblasting is beneficial to achieving thicker HA coatings on the target surface. The results are consistent with the previous studies, in which the thick HA coatings were obtained on the sandblasted commercial Ti6Al4V alloy coupons [46, 62]. The cross-section SEM images also revealed that dense HA coating was achieved on the surface without compromising substrate

properties, as no noticeable crack or fracture was detected on the DED-printed cp-Ti metal parts after the CS process.

The crystalline structure of HA was preserved after cold spraying according to the XRD analysis in Fig. 9. Four different XRD analysis results are shown in Fig. 9: (i) the DED-printed cp-Ti surface, (ii) HA powder, (iii) CS HA coating on the face-milled cp-Ti surface, and (iv) CS HA coating on the sandblasted cp-Ti surface. It is noted that the CS HA coating on the sandblasted cp-Ti surface showed the attenuated intensity of major Ti peaks (38.46° and 40.19°) while preserving sharp HA peaks (between 45° and 55°). On the other hand, the CS HA coating on the face-milled cp-Ti surface showed relatively high major Ti peaks (38.46° and 40.19°). Results indicate that dense and thick HA over-coating with implant-friendly crystalline structure was achieved on the sandblasted cp-Ti surface by cold spraying.

Figure 10 shows the pull-off adhesion test results for the HA-coated samples with different pre-surface treatments (i.e., face milled and sandblasted). The sandblasted cp-Ti surfaces resulted in significantly greater adhesion strength (i.e., > 40%) than the face-milled cp-Ti surfaces, which is likely attributed to proper anchoring of the impinging particles onto/into the troughs on the sandblasted cp-Ti surface.

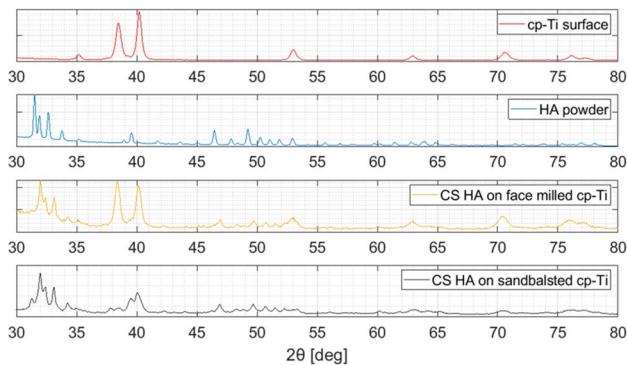
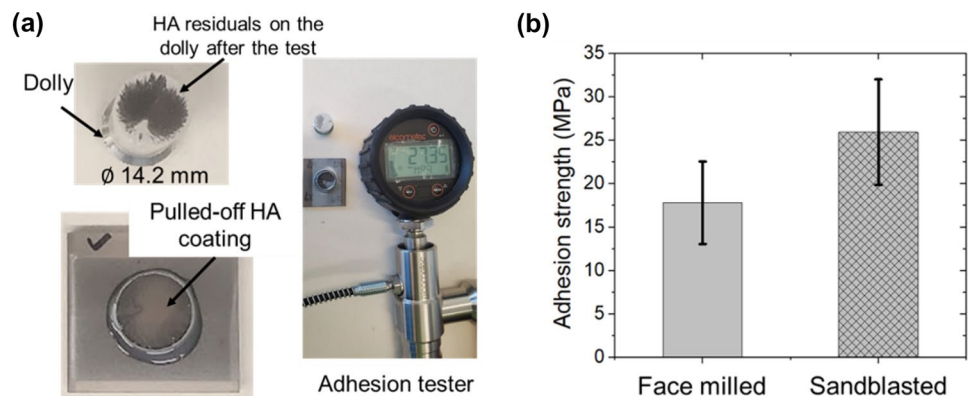


Fig. 9 XRD analysis of DED-printed cp-Ti surface, HA powder, CS HA on the face-milled cp-Ti surface, and CS HA on sandblasted cp-Ti surface

Fig. 10 **a** Adhesion test dolly (upper left panel), pulled-off specimen (bottom left panel), and adhesion tester (right panel); **b** adhesion strength of the resulting cold-sprayed HA coatings on the Ti substrates with different surface conditions



The maximum adhesion strength of HA coating on the sandblasted specimens was obtained to be 34.78 MPa while the minimum strength was 19.16 MPa. Considering the ISO-13779 standard (i.e., implants for surgery—hydroxyapatite) [65], which suggests that no individual result shall be less than 10 MPa and the average coating strength should exceed 15 MPa, the resultant HA coating through cold spraying on sandblasted cp-Ti surfaces is promising in terms of adhesion strength for orthopedic implant applications. Taken together, the results suggest that, before cold spraying, processing of the DED-printed cp-Ti surface by sandblasting is critical not only to achieving a dense HA coating with less porosity but also to obtaining sufficient adhesion strength for effective orthopedic implant applications. As such, the functional HA coatings on sandblasted cp-Ti surfaces were subsequently used for the biological test, in vitro Ni ion release.

3.4 Ni ion leaching test results

A total of 18 test samples of 4 types were prepared as shown in Fig. 5. Nitinol samples (S1) were machined after the DED process and subsequent heat treatments. The other samples (S2 and S3) were prepared by depositing coatings on the S1 samples. The Ni ion release amount was analyzed by measuring the Ni concentration in the $1 \times$ PBS solution that contained each sample for 3 days. The average Ni concentration measurement test results for each sample type are shown in Fig. 11. It should be noted that Ni concentration from S1 and S2 samples decreased from the '1–3 days' (S1: 0.418 ng/ml/mm² and S2: 0.439 ng/ml/mm²) to the '7–9 days' (S1: 0.058 ng/ml/mm² and S2: 0.055 ng/ml/mm²). After 30 days, the Ni concentration from S1 and S2 was reduced to the level of S3. The S3 sample showed a very low Ni concentration (0.009–0.034 ng/ml/mm²) throughout the experiment period. The Ni ion release rate from this study was compared to that of commercially produced orthodontic Nitinol wires as shown in Table 4. The Ni release rates from this study were comparable to that of commercial Nitinol wires with the lowest Ni ion release rate. It should be noted that

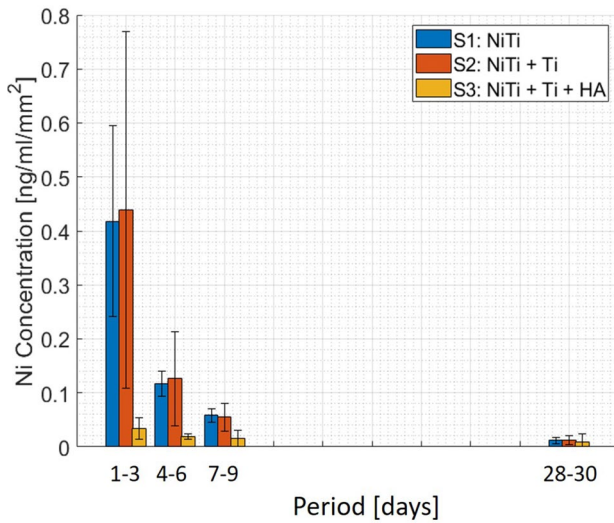


Fig. 11 Ni concentration in the PBS solution from test period days

the commercial Nitinol wires released more Ni ions with a shorter period of immersion time, 9 days for this study and 7 days for reference cases. Especially, the S3 samples showed a Ni release rate that is an order of magnitude smaller compared to commercial Nitinol wires. The effect of the pH level of the immersion solution on the Ni release rate should be carefully considered since the pH levels of immersion solutions are different in Table 4. The study by Huang et al. [66] in Table 4 shows the Ni release rates from immersion solutions with pH levels of 5.0 and 6.25 are almost the same. Sussman et al. [67] showed that the Ni release rates from Nitinol from immersion solutions with

pH levels of 6.25 and 7.2 showed a 19–96% of difference. Even with the maximum difference of 96%, Table 4 clearly shows that the Nitinol structures from this study are safer in the aspect of Ni ion release, compared to commercial orthodontic Nitinol wires.

The Ni concentration from S2 was slightly higher compared to S1 at the beginning of immersion. To explain the result, the side surfaces of all samples and their phase distribution were analyzed. The side surfaces of different types of samples after 30 days of the experiment are shown in Fig. 12. Due to additional Ti gradient layers on the top and bottom of the Nitinol disk, the side surface area of S2 was twice larger compared to S1. As shown in Fig. 7, the side surface is mainly composed of cp-Ti, but there are NiTi₂ phases mixed in the cp-Ti matrix. It was reported that the NiTi₂ phase showed lower erosion resistance than that of the NiTi phase [68]. Therefore, an increased Ni concentration from S2 may be explained by the presence of the NiTi₂ phase, especially dense thin layers (~20 microns) formed on top and bottom of the Nitinol disk. It should be noted that (i) the thickness of the Ti gradient layer is relatively large only when the sample is small, and (ii) the side surface is exposed only with limited sample geometry. In a realistic size scale, as demonstrated in Fig. 1, the thickness of the Ti gradient layer is negligible and the side surface is not exposed.

As for future work, the authors will evaluate the developed Nitinol structure in terms of biocompatibility through additional in vitro and in vivo tests. We envision that, owing to its negligible nickel ion release and promising bond strength, the novel Nitinol structure that was developed in this study will have wide utility as implantable material over conventional metals.

Table 4 Accumulated Ni release amount [$\mu\text{g}/\text{cm}^2$] compared with commercial orthodontic Nitinol wires

Source	Nitinol samples from different vendors	Test period [days]	Immersion solution	Accumulated Ni release amount [$\mu\text{g}/\text{cm}^2$]
This study	S1 (NiTi)	9	PBS (pH: 7.4)	0.178
	S2 (NiTi + Ti)			0.130
	S3 (NiTi + Ti + HA)			0.036
Arndt et al. [69]	Titanol Low force	7	Artificial saliva (pH: 5.0)	1.9
	Tensic			0.4
	Euro Arch			0.2
	Nitinol Classic			0.1
Huang et al. [66]	Ormco	7	Custom (pH: 5.0)	0.92
	RMO Inc			2.33
	Shin-Ya Co			1.58
	Kuo-Hua Co			0.78
Huang et al. [66]	Ormco	7	Custom (pH: 6.25)	0.92
	RMO Inc			2.49
	Shin-Ya Co			1.92
	Kuo-Hua Co			0.45

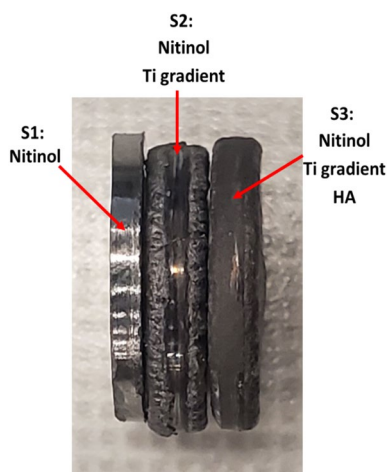


Fig. 12 Side surfaces of three different samples after the in vitro testing for 30 days

4 Conclusion

In this study, a novel method of building functionally gradient layers on Nitinol using additive manufacturing processes (the DED and the cold spray) was presented. The entire Nitinol structure could reduce the stress shielding effects and suppress potentially toxic Ni ion release from the Nitinol surface, providing more advantageous features in medical implant applications. The following conclusions can be drawn from this study.

- A Nitinol structure with its Young's modulus (60 GPa) closely matching that of human bones (30 GPa) was prepared using the DED technique and post-heat treatment. The microstructure of the Nitinol showed a high purity of the NiTi phase without any microstructural defects such as pores and cracks.
- The functional Ti gradient layer on the Nitinol surface showed a 0% Ni composition that can suppress Ni ion release. The entire coating thickness of the gradient layer was suppressed within 500 microns to ensure the mechanical properties of the core Nitinol are preserved. The highest level of bonding strength was achieved in the gradient layer due to the complete alloyed microstructure without microstructural defects.
- Additional biomedical over-coating (HA) for enhanced biocompatibility was deposited on the cp-Ti layer using the cold spray technique. A promising adhesion strength (26 MPa) of HA over-coating on the cp-Ti surface was achieved, which exceeded the requirement by the ISO-13779 standard (15 MPa) for orthopedic implant applications.
- The in vitro Ni ion release from uncoated and coated Nitinol samples was analyzed. Both the uncoated and Ti-

coated Nitinol samples showed the Ni release rate comparable to commercial orthodontic Nitinol wires. Especially, additional HA-coated Nitinol samples showed the Ni release rate which is an order of magnitude smaller than that of commercial orthodontic Nitinol wires.

Acknowledgements The authors wish to gratefully acknowledge the financial support provided for this study by the National Science Foundation (Grant No. CMMI-1233783).

Declarations

Conflict of interest On behalf of all authors, the corresponding author states that there is no conflict of interest.

References

1. Kang C-W, Fang F-Z (2018) State of the art of bioimplants manufacturing: part I. *Adv Manuf* 6(1):20–40
2. Kamachimudali U, Sridhar TM, Raj B (2003) Corrosion of bio implants. *Sadhana* 28(3):601–637
3. Niinomi M, Nakai M, Hieda J (2012) Development of new metallic alloys for biomedical applications. *Acta Biomater* 8(11):3888–3903
4. Lemons JE, Niemann KMW, Weiss AB (1976) Biocompatibility studies on surgical-grade titanium-, cobalt-, and iron-base alloys. *J Biomed Mater Res* 10(4):549–553
5. Sudarshan TS, Srivatsan TS, Harvey Ii DP (1990) Fatigue processes in metals—role of aqueous environments. *Eng Fract Mech* 36(6):827–852
6. Lei MK, Zhu XM (2001) In vitro corrosion resistance of plasma source ion nitrided austenitic stainless steels. *Biomaterials* 22(7):641–647
7. Chen Q, Thouas GA (2015) Metallic implant biomaterials. *Mater Sci Eng R Rep* 87:1–57
8. Priyadarshini B, Rama M, Chetan, Vijayalakshmi U (2019) Bioactive coating as a surface modification technique for biocompatible metallic implants: a review. *J Asian Ceram Soc* 7(4):397–406
9. Lane JM, Mait JE, Unnanuntana A, Hirsch BP, Shaffer AD, Shonuga OA (2011) *Materials in fracture fixation*. Elsevier
10. Patel NR, Gohil PP (2012) A review on biomaterials: scope, applications & human anatomy significance. *Int J Emerg Technol Adv Eng* 2(4):91–101
11. Aihara H, Zider J, Fanton G, Duerig T (2019) Combustion synthesis porous nitinol for biomedical applications. *Int J Biomater* 2019:1–11
12. Shayesteh-Moghaddam N, Taheri-Andani M, Amerinatanzi A, Haberland C, Huff S, Miller M, Elahinia M, Dean D (2016) Metals for bone implants: safety, design, and efficacy. *Biomaterials* 1(1):1–16
13. Khalil-Allafi J, Amin-Ahmadi B, Zare M (2010) Biocompatibility and corrosion behavior of the shape memory NiTi alloy in the physiological environments simulated with body fluids for medical applications. *Mater Sci Eng, C* 30(8):1112–1117
14. Bernard SA, Balla VK, Davies NM, Bose S, Bandyopadhyay A (2011) Bone cell-materials interactions and Ni ion release of anodized equiatomic NiTi alloy. *Acta Biomater* 7(4):1902–1912
15. Li CY, Yang XJ, Zhang LY, Chen MF, Cui ZD (2007) In vivo histological evaluation of bioactive NiTi alloy after two years implantation. *Mater Sci Eng, C* 27(1):122–126

16. Ryhänen J, Niemi E, Serlo W, Niemelä E, Sandvik P, Pernu H, Salo T (1997) Biocompatibility of nickel-titanium shape memory metal and its corrosion behavior in human cell cultures. *J Biomed Mater Res* 35(4):451–457
17. Ryhänen J, Kallioinen M, Tuukkanen J, Junila J, Niemelä E, Sandvik P, Serlo W (1998) In vivo biocompatibility evaluation of nickel-titanium shape memory metal alloy: Muscle and perineural tissue responses and capsule membrane thickness. *J Biomed Mater Res* 41(3):481–488
18. Ryhänen J, Kallioinen M, Tuukkanen J, Lehenkari P, Junila J, Niemelä E, Sandvik P, Serlo W (1999) Bone modeling and cell–material interface responses induced by nickel–titanium shape memory alloy after periosteal implantation. *Biomaterials* 20(14):1309–1317
19. Wever DJ, Veldhuizen AG, Sanders MM, Schakenraad JM, Van Horn JR (1997) Cytotoxic, allergic and genotoxic activity of a nickel–titanium alloy. *Biomaterials* 18(16):1115–1120
20. Trepanier C, Leung TK, Tabrizian M, Yahia LH, Biennu JG, Tanguay JF, Piron DL, Bilodeau L (1999) Preliminary investigation of the effects of surface treatments on biological response to shape memory NiTi stents. *J Biomed Mater Res* 48(2):165–171
21. Ayers RA, Simske SJ, Bateman TA, Petkus A, Sachdeva RLC, Gyunter VE (1999) Effect of nitinol implant porosity on cranial bone ingrowth and apposition after 6 weeks. *J Biomed Mater Res* 45(1):42–47
22. Wataha JC, Lockwood PE, Marek M, Ghazi M (1999) Ability of Ni-containing biomedical alloys to activate monocytes and endothelial cells in vitro. *J Biomed Mater Res* 45(3):251–257
23. Shih CC, Lin SJ, Chen YL, Su YY, Lai ST, Wu GJ, Kwok CF, Chung KH (2000) The cytotoxicity of corrosion products of nitinol stent wire on cultured smooth muscle cells. *J Biomed Mater Res* 52(2):395–403
24. Hassani M, Mousavi SA, Entezami SS (2012) The control process of nitinol alloy drilling through fuzzy logic. *Majlesi J Mechatron Syst* 1(2):1–7
25. Malukhin K, Ehmann K (2006) Material characterization of NiTi based memory alloys fabricated by the laser direct metal deposition process. *J Manuf Sci Eng* 128(3):691–696
26. Halani P, Shin Y (2012) In situ synthesis and characterization of shape memory alloy nitinol by laser direct deposition. *Metall and Mater Trans A* 43A(2):650–657
27. Khademzadeh S, Parvin N, Bariani P (2015) Production of NiTi alloy by direct metal deposition of mechanically alloyed powder mixtures. *Int J Precis Eng Man* 16(11):2333–2338
28. Shishkovsky I, Yadroitsev I, Smurov I (2012) Direct selective laser melting of nitinol powder. *Phys Procedia* 39:447–454
29. Gureev D, Emelina O, Zhuravel L, Petrov A, Pokoev A, Shishkovsky I (2002) Structure and properties of Ni-Ti intermetallic phases synthesized upon selective laser sintering: I. X-ray diffraction analysis. *Phys Metals Metallogr* 93(2):180–184
30. Shishkovsky I, Volova L, Kuznetsov M, Morozov Y, Parkin I (2008) Porous biocompatible implants and tissue scaffolds synthesized by selective laser sintering from Ti and NiTi. *J Mater Chem* 18(12):1309–1317
31. Zhou Q, Hayat MD, Chen G, Cai S, Qu X, Tang H, Cao P (2019) Selective electron beam melting of NiTi: microstructure, phase transformation and mechanical properties. *Mater Sci Eng, A* 744:290–298
32. Otubo J, Rigo OD, Neto CM, Mei PR (2006) The effects of vacuum induction melting and electron beam melting techniques on the purity of NiTi shape memory alloys. *Mater Sci Eng, A* 438:679–682
33. Otubo J, Rigo OD, Moura-Neto CD, Kaufman MJ, Mei PR (2004) Low carbon content NiTi shape memory alloy produced by electron beam melting. *Mater Res* 7(2):263–267
34. Bernard S, Balla V, Bose S, Bandyopadhyay A (2011) Rotating bending fatigue response of laser processed porous NiTi alloy. *Mater Sci Eng C* 31(4):815–820
35. Bernard S, Balla V, Bose S, Bandyopadhyay A (2012) Compression fatigue behavior of laser processed porous NiTi alloy. *J Mech Behav Biomed Mater* 13:62–68
36. Saedi S, Turabi A, Andani M, Haberland C, Karaca H, Elahinia M (2016) The influence of heat treatment on the thermomechanical response of Ni-rich NiTi alloys manufactured by selective laser melting. *J Alloys Compd* 677:204–210
37. Lee J, Shin YC (2019) Effects of composition and post heat treatment on shape memory characteristics and mechanical properties for laser direct deposited nitinol. *Lasers Manuf Mater Process* 6(1):41–58
38. Ahadi A, Sun Q (2013) Stress hysteresis and temperature dependence of phase transition stress in nanostructured NiTi—Effects of grain size. *Appl Phys Lett* 103(2):021902
39. Sun B, Fu MW, Lin JP, Ning YQ (2017) Effect of low-temperature aging treatment on thermally-and stress-induced phase transformations of nanocrystalline and coarse-grained NiTi wires. *Mater Des* 131:49–59
40. Shabalovskaya SA (2002) Surface, corrosion and biocompatibility aspects of Nitinol as an implant material. *Bio-Med Mater Eng* 12(1):69–109
41. Kuphasuk C, Oshida Y, Andres CJ, Hovijitra ST, Barco MT, Brown DT (2001) Electrochemical corrosion of titanium and titanium-based alloys. *J Prosthet Dent* 85(2):195–202
42. Li C-J, Li W-Y (2003) Deposition characteristics of titanium coating in cold spraying. *Surf Coat Technol* 167(2):278–283
43. Walsh WR, Bertollo N, Christou C, Schaffner D, Mobbs RJ (2015) Plasma-sprayed titanium coating to polyetheretherketone improves the bone-implant interface. *Spine J* 15(5):1041–1049
44. Maleki-Ghaleh H, Khalil-Allafi J (2019) Characterization, mechanical and in vitro biological behavior of hydroxyapatite-titanium-carbon nanotube composite coatings deposited on NiTi alloy by electrophoretic deposition. *Surf Coat Technol* 363:179–190
45. Guillem-Martí J, Cinca N, Punset M, Cano IG, Gil FJ, Guilemany JM, Dosta S (2019) Porous titanium-hydroxyapatite composite coating obtained on titanium by cold gas spray with high bond strength for biomedical applications. *Colloids Surf, B* 180:245–253
46. Vilardell AM, Cinca N, Cano IG, Concustell A, Dosta S, Guilemany JM, Estradé S, Ruiz-Caridad A, Peiró F (2017) Dense nanostructured calcium phosphate coating on titanium by cold spray. *J Eur Ceram Soc* 37(4):1747–1755
47. Nagano M, Nakamura T, Kokubo T, Tanahashi M, Ogawa M (1996) Differences of bone bonding ability and degradation behaviour in vivo between amorphous calcium phosphate and highly crystalline hydroxyapatite coating. *Biomaterials* 17(18):1771–1777
48. Overgaard S, Bromose U, Lind M, Bünger C, Søballe K (1999) The influence of crystallinity of the hydroxyapatite coating on the fixation of implants: mechanical and histomorphometric results. *J Bone Jt Surg Brit* 81(4):725–731
49. Burgess AV, Story BJ, Wagner WR, Trisi P, Pikos MA, Guttenberg SA (1999) Highly crystalline MP-1 hydroxylapatite coating Part II: in vivo performance on endosseous root implants in dogs. *Clin Oral Implant Res* 10(4):257–266
50. Yu-Liang C, Lew D, Park JB, Keller JC (1999) Biomechanical and morphometric analysis of hydroxyapatite-coated implants with varying crystallinity. *J Oral Maxillofac Surg* 57(9):1096–1108
51. Xue W, Liu X, Zheng X, Ding C (2005) Effect of hydroxyapatite coating crystallinity on dissolution and osseointegration in vivo. *J Biomed Mater Res Part A* 74(4):553–561

52. Tsai J-T, Akin S, Zhou F, Bahr DF, Jun MB-G (2021) Establishing a cold spray particle deposition window on polymer substrate. *J Therm Spray Technol* 30(4):1069–1080
53. Sova A, Smurov I, Doubenskaia M, Petrovskiy P (2018) Deposition of aluminum powder by cold spray micronozzle. *Int J Adv Manuf Technol* 95(9):3745–3752
54. P. ASTM Int West Conshohocken, 2002, <https://www.astm.org> 2002:1–10, ASTM D4541-95e1. Standard Test Method for Pull-Off Strength of Coatings Using Portable Adhesion Testers
55. Tsai J-T, Akin S, Zhou F, Park MS, Bahr DF, Jun MB-G (2022) Electrically conductive metallized polymers by cold spray and co-electroless deposition. *ASME Open J Eng* 1:011007
56. Melentiev R, Yu N, Lubineau G (2021) Polymer metallization via cold spray additive manufacturing: a review of process control, coating qualities, and prospective applications. *Addit Manuf* 48:102459
57. Graziani G, Boi M, Bianchi M (2018) A review on ionic substitutions in hydroxyapatite thin films: towards complete biomimetism. *Coatings* 8(8):269
58. Kravanja KA, Finšgar M (2021) Analytical techniques for the characterization of bioactive coatings for orthopaedic implants. *Biomedicines* 9(12):1936
59. Technical Considerations for Non-Clinical Assessment of Medical Devices Containing Nitinol: Guidance for Industry and Food and Drug Administration Staff, 2021
60. Zhang L, He ZY, Tan J, Zhang YQ, Stoica M, Calin M, Prashanth KG, Cordill MJ, Jiang YH, Zhou R, Eckert J (2017) Designing a novel functional-structural NiTi/hydroxyapatite composite with enhanced mechanical properties and high bioactivity. *Intermetallics* 84:35–41
61. Abioye TE, Farayibi PK, Kinnel P, Clare AT (2015) Functionally graded Ni-Ti microstructures synthesised in process by direct laser metal deposition. *Int J Adv Manuf Technol* 79(5):843–850
62. Vilardell AM, Cinca N, Dosta S, Cano IG, Guilemany JM (2019) Feasibility of using low pressure cold gas spray for the spraying of thick ceramic hydroxyapatite coatings. *Int J Appl Ceram Technol* 16(1):221–229
63. Akin S, Wu P, Tsai J-T, Nath C, Chen J, Jun MB-G (2021) A study on droplets dispersion and deposition characteristics under supersonic spray flow for nanomaterial coating applications. *Surf Coat Technol* 426:127788
64. Jen T-C, Li L, Cui W, Chen Q, Zhang X (2005) Numerical investigations on cold gas dynamic spray process with nano-and micro-size particles. *Int J Heat Mass Transf* 48(21–22):4384–4396
65. ISO 13779-2 Implants for surgery—hydroxyapatite—{Part} 2: {Thermally} sprayed coatings of hydroxyapatite 2008
66. Huang H-H, Chiu Y-H, Lee T-H, Wu S-C, Yang H-W, Su K-H, Hsu C-C (2003) Ion release from NiTi orthodontic wires in artificial saliva with various acidities. *Biomaterials* 24(20):3585–3592
67. Sussman EM, Shi H, Turner PA, Saylor DM, Weaver JD, Simon DD, Takmakov P, Sivan S, Shin HY, Di Prima MA (2022) Nitinol release of nickel under physiological conditions: effects of surface oxide, pH hydrogen peroxide, and sodium hypochlorite. *Shape Mem Superelast* 8:1–9
68. Hiraga H, Inoue T, Shimura H, Matsunawa A (1999) Cavitation erosion mechanism of NiTi coatings made by laser plasma hybrid spraying. *Wear* 231(2):272–278
69. Arndt M, Brück A, Scully T, Jäger A, Bourauel C (2005) Nickel ion release from orthodontic NiTi wires under simulation of realistic in-situ conditions. *J Mater Sci* 40(14):3659–3667

Publisher's Note Springer Nature remains neutral with regard to jurisdictional claims in published maps and institutional affiliations.

Springer Nature or its licensor (e.g. a society or other partner) holds exclusive rights to this article under a publishing agreement with the author(s) or other rightsholder(s); author self-archiving of the accepted manuscript version of this article is solely governed by the terms of such publishing agreement and applicable law.